Effects of Geometric Curvature on Electron Flows at the Onset of Fluidity in Nanoscale Materials

James Capers
(Supervisor: Andrey Shytov)
School of Physics, University of Exeter

(Dated: April 26, 2019)

Viscous electron fluids have recently emerged as a way of explaining the transport of strongly interacting electrons in clean nanoscale materials. Recent studies of the genesis of this fluidity, and the effect of curved current injectors present an interesting open question: how is electron flow at the onset of fluidity affected by geometric curvature of current injectors at the boundary? Using complex analysis to reformulate the Boltzmann kinetic equation, we numerically solve this problem for semi-elliptical and a semi-circular "groove" current injectors, to provide some of the first insight into viscous effects caused by geometric curvature at the onset of fluidity. We demonstrate that effects predicted by hydrodynamic theory are also present at the very onset of fluidity, caused by electrons moving against the electrical potential, manifesting as voltage suppression at the tip of the needle and a build up of charge inside the "groove" cavity. These effects are found to depend strongly upon geometric curvature, and become more pronounced as electron-electron mean free path is decreased, although there are hints that interaction driven effects could be maximal at intermediate mean free paths, dictated by the exact geometry.

Contents

I.   Introduction

Electron transport in metals is usually dominated by inelastic scattering with phonons or lattice impurities. However more exotic transport regimes have long been predicted [1–5], but have until recently eluded experimental observation. The emergence of these new transport regimes in metals can be understood by considering the interplay between three length scales. The electron-electron mean free path, ℓ_{ee}, describes the distance between electron-electron collisions, which conserve momentum. The electron-phonon and electron-impurity mean free path ℓ_{e-ph}, gives the length scale at which electron momentum is relaxed, and L is the size of the system. For normal Ohmic transport $\ell_{e-ph} < \ell_{ee}, L$ so that electron momentum is relaxed very quickly, giving transport described by Drude theory [6]. On the other hand if electron-electron and electron-impurity scattering events occur at length scales larger than the size of the system, $L < \ell_{ee}, \ell_{e-ph}$, then transport is ballistic and described by the collisionless Boltzmann equation [7]. Lastly, since carrier interactions are elastic, if these are the dominant interaction mechanism, $\ell_{ee} < \ell_{e-ph}, L$, then the resulting electron system can be described using hydrodynamic theory [8], since it macroscopically conserves energy and momentum. Recent advances in producing systems where electron-electron interactions are very strong or scattering due to impurities and phonons is weak, has led to the direct observation of electron fluids. These strange systems may exhibit many hydrodynamic phenomena such as vortices [9, 10], whirlpools [11, 12], Poiseuille flow [13, 14] as well as higher than ballistic conduction [15] and the breakdown of the Wiedemann-Franz law [16]. Such phenomena are observed in a growing collection of clean metallic systems, such as GaAs [1] and $PdCoO_2$ [13] as well as graphene [9–12, 16–18]. Graphene presents a particularly good venue to observe hydrodynamic electron transport due to its very clean crystal structure [19] and suppressed phonon interactions [20, 21]. Recent studies of phenomena caused by strong carrier interactions[9, 10] show that the electron fluid in graphene can be described by low Reynolds number hydrodynamics [22], stated as the Ohm-Stokes equation along with the usual incompressibility condition

$$(\eta\nabla^2 - n^2e^2\rho)\mathbf{v} = ne\nabla\phi, \qquad \nabla \cdot \mathbf{v} = 0, \qquad (1.1)$$

where η is the viscosity, n is electron density, e is the electronic charge, ρ is resistivity, $\mathbf{v}$ is the electron velocity and ϕ is the electrical potential. This is simply the Stokes equation with an added Ohmic relaxation term, which becomes dominant at length scales $\xi = \sqrt{\ell_{ee}\ell_{e-ph}}$ [10]. One should notice that in the absence of viscosity $\eta = 0$, this is simply Ohm's law and in the absence of Ohmic resistivity $\rho = 0$ this is the Stokes equation. This has been used to show, both theoretically and experimentally, that in strongly interacting electron fluids the effect of carrier interactions is to de-couple current

and potential, resulting in non-local responses which can manifest as electrons flowing against the potential [9, 10], resulting in regions of negative potential near source or positive potential near drain contacts [9–11, 14, 19, 23]. However, since graphene's carrier density can be easily gate tuned [10, 24], even richer physics may be observed. Both the ballistic and hydrodynamic length scale inequalities may be satisfied in the same sample. This has facilitated the exploration of the transition from ballistic to hydrodynamic flow, where it has been shown that the effects of carrier interactions are maximal at the crossover [25, 26]. It should be noted that in terms of the three key length scales, the onset of fluidity occurs at $\ell_{ee} \sim L$ and $L, \ell_{ee} < \ell_{e-ph}$: as the electron system moves from ballistics to hydrodynamics. Separately, curved current injectors placed inside an electron fluid have been considered, where the effect of geometric curvature upon potential distributions and flow patterns in the hydrodynamic regime was investigated [27]. It was shown that curvature of current injecting electrons can have a large effect upon the flow patterns and the potential. For example, a large voltage suppression at the tip of elliptical contacts is predicted by the fully hydrodynamic treatment.

We aim to extend understanding into the gap presented by recent works: the onset of fluidity on curved geometries. To do this, we must answer the following questions: are the hydrodynamic effects predicted on curved geometries by the Stokes equation [27] also observed at the onset of fluidity? How do these effects depend upon parameters of the geometry and electron-electron mean free path? When could these effects be maximally observed in experiment? This work aims to answer these questions, by applying a fully kinetic treatment to curved current injector geometries located at the boundary, rather than in the bulk as recent hydrodynamic studies have considered [27], since this is a more experimentally realistic configuration. Of particular interest are elliptic current injectors, since this type of contact is useful for imaging the electron flows [28, 29], hence this is where most attention has been focused, although it should be noted that our model is easily extendable to many other curved geometries and is not limited to either the ballistic or hydrodynamic limits.

The rest of this report is laid out as follows. In Section II i we outline standard kinetic theory, and how this may be applied to an electron gas on the Fermi surface. The connection between kinetics and experimentally measurable quantities is also explained, along with how collisions in the bulk (away from boundaries) are treated within this framework. Then in Section II ii we present our own reformulation of the kinetic equation to treat curved geometries, and explain the motivation behind these analytic results. Section II iii then explains the boundary conditions that are applied, and the assumptions behind them, in order to solve the kinetic equation on curved geometries. The numerical solution of this system is then outlined in Section III, before the results are presented and discussed in Section IV.

II. Theory

II.i. Kinetics

To explore the onset of fluidity, as well as the ballistic and hydrodynamic regimes, we consider the kinetics of electrons in a Fermi gas using the Boltzmann kinetic equation. The application of kinetics to this problem is motivated by the limitations of the Ohm-Stokes model (1.1). Since it is a hydrodynamic model, it is valid only in the limit $\ell_{ee} \to 0$. While it is possible to probe this experimentally, in the hydrodynamic regime contact resistance R_V scales as $R_V \propto \eta \propto \ell_{ee}$ [9] meaning that as $\ell_{ee} \to 0$, $\phi \to 0$ making the effects difficult to probe. Since the kinetic formalism does not only work in this limit, a much larger range of mean free paths can be treated, widening the range of systems, temperatures and dopings to which this model might be applicable. With this motivation, the Boltzmann kinetic equation [7] can be written most generally as

$$\mathcal{I}[f] = \frac{\partial f}{\partial t} + \mathbf{v} \cdot \nabla f + \mathbf{F} \cdot \frac{\partial f}{\partial \mathbf{p}}, \tag{2.1}$$

where f is the distribution function, $\mathbf{v}$ is particle velocity, $\mathbf{p}$ is particle momentum and $\mathbf{F} = -\nabla U(\mathbf{r})$ is the force due to a general external potential $U(\mathbf{r})$. Physically, f represents the number of particles inside a given phase space volume, $d\mathbf{r}d\mathbf{p}$, so that the total number of particles is given by

$$N = \int f d\mathbf{r}d\mathbf{p}, \tag{2.2}$$

which in two dimensions is a four dimensional integral over the x and y components of position and momentum. The relaxation or redirection of particle momentum is described by the collision integral $\mathcal{I}[f]$. Since we consider the case of two-dimensional nanomaterials (such as graphene), we can confine our analysis to two dimensions (the $x - y$ plane). The distribution function is in general a function of position, momentum, energy and time, $f = f(\mathbf{r}, \mathbf{p}, \varepsilon, t)$, however we apply several important assumptions to simplify this.

Firstly, we consider only steady state solutions, so that f has no time dependence. This reduces dimensionality from 6 dimensions to 5 dimensions $f(\mathbf{r}, \mathbf{p}, \varepsilon, t) \to f(\mathbf{r}, \mathbf{p}, \varepsilon)$. Next, due to collinear scattering [30, 31], energy is relaxed more quickly than momentum so we can assume that all electrons at the Fermi level have the same energy, $\varepsilon \approx E_F$, thus we can also neglect the energy dependence of the electrons. This further reduces the distribution we consider from 5 dimensions to 4, $f(\mathbf{r}, \mathbf{p}, \varepsilon) \to f(\mathbf{r}, \mathbf{p})$. The assumption that electron energies are the same also allows us to specify the electron momentum as $p_x = mv_F \cos\theta$, $p_y = mv_F \sin\theta$, where v_F is the Fermi velocity. Momentum is therefore parametrised by the single variable θ, which is the propagation direction on the 2D Fermi surface, $\theta = \arctan(y/x)$. This leaves us with a three dimensional problem $f(\mathbf{r}, \mathbf{p}) \to f(\mathbf{r}, \theta)$. The reduction of dimensionality is important, since it lets us move from a problem which is practically intractable to numerical solution, to a problem which is manageable. For convenience, we shall work in units where electron momentum is equal to one.

The distribution function $f(\mathbf{r}, \theta)$ represents the deviation from the equilibrium distribution f_0, giving the total distribution, $\tilde{f}$ as

$$\tilde{f} = f_0 - f, \tag{2.3}$$

where the equilibrium distribution is simply the Fermi-Dirac distribution

$$f_0 = \frac{1}{e^{(\varepsilon-\mu)/k_B T} + 1}. \tag{2.4}$$

Solving (2.1) under these assumptions for the perturbation to the equilibrium distribution, f, permits the calculation of experimentally measurable quantities such as potential and current. If the angular average of the distribution is defined as

$$\langle f \rangle \equiv \int_0^{2\pi} f(\mathbf{r}, \theta) \frac{d\theta}{2\pi}, \tag{2.5}$$

then charge and current densities can be found by calculating moments of the distribution function using this definition

$$\rho(\mathbf{r}) = \langle f(\mathbf{r}, \theta) \rangle, \tag{2.6}$$
$$\mathbf{j}(\mathbf{r}) = \langle \mathbf{v} f(\mathbf{r}, \theta) \rangle, \tag{2.7}$$

where $\rho(\mathbf{r})$ and $\mathbf{j}(\mathbf{r})$ are the charge and current densities respectively. Current density can then be related to the stream function, ψ, [22] using

$$j_x = ne\frac{\partial \psi}{\partial y}, \qquad j_y = -ne\frac{\partial \psi}{\partial x}. \tag{2.8}$$

Isolines of the stream function describe electron trajectories, providing a useful visualisation tool when analysing flow patterns, as ψ represents the volume flux of particles.

To related charge density to electrical potential, $\phi(\mathbf{r})$, we use the Thomas-Fermi screening approximation [6, 32]. The key assumptions of this model are that the applied electrical field, ϕ is weak and slowly varying in space. This approximation also assumes electrical neutrality at distances larger than the screening radius and imposes that the electrical potential must compensate exactly the charge density, allowing the potential to be determined from charge density via

$$\phi(\mathbf{r}) = -\frac{1}{e^2\nu}\rho(\mathbf{r}), \tag{2.9}$$

where e is the charge of an electron and ν is the density of states at the Fermi level. This allows the charge density

we calculate to be connected to experimental measurements of potential via a constant, which depends upon the experimental system.

An important aspect of the kinetic model is the collision integral, $\mathcal{I}[f]$. This allows the type of collision (momentum conserving, momentum non-conserving or both) being considered to be changed, and the strength of these collisions set by the scattering rate γ. This collision rate is related to the mean free path as $\ell = v_F/\gamma$, where γ_{ee} gives the rate of electron-electron collisions and γ_{e-ph} is the rate of electron-phonon or electron impurity collisions. The form of the collision integral used is

$$\mathcal{I}[f] = -(\gamma_{ee} + \gamma_{e-ph})(f - \langle f \rangle) - 2\gamma_{ee}\hat{v} \times \langle \hat{v}f \rangle, \quad (2.10)$$

where $\hat{v} = (\cos\theta, \sin\theta)$. The collision integral can be understood by decomposing it into the Ohmic and viscous parts

$$\mathcal{I}_{\text{Ohmic}}[f] = -\gamma_{e-ph}(f - \langle f \rangle), \quad (2.11)$$
$$\mathcal{I}_{\text{viscous}}[f] = -\gamma_{ee}(f - \langle f \rangle) - 2\gamma_{ee}\hat{v} \times \langle \hat{v}f \rangle, \quad (2.12)$$

so that the total collision integral is simply a linear combination of the two $\mathcal{I}[f] = \mathcal{I}_{\text{Ohmic}}[f] + \mathcal{I}_{\text{viscous}}[f]$.

The Ohmic collision integral is simply the well known relaxation time approximation [6, 32], which describes collisions with phonons or impurities, relaxing electron momentum at length scales ℓ_{e-ph}. This conserves only the first harmonic $\mathcal{I}_{\text{Ohmic}}[1] = 0$, meaning that particle number (or charge) is conserved but momentum is not. This leads to classical Ohmic behaviour, with electrons propagating according to Ohm's law. For the viscous collision integral we use a form [1, 33, 34] which conserves the first three harmonics $\mathcal{I}_{\text{viscous}}[1] = \mathcal{I}_{\text{viscous}}[\cos\theta] = \mathcal{I}_{\text{viscous}}[\sin\theta] = 0$, meaning that x and y momentum as well as particle number are conserved. This collision integral does not relax momentum, but just re-directs electron trajectories. The collision integral (2.10) allows the mixed Ohmic-viscous behaviour given by solving (1.1) to be studied using the kinetic treatment, as well as either Ohmic or viscous behaviour in isolation by setting γ_{ee} or γ_{e-ph} to zero. Additionally, since the strength of electron-electron interactions can be directly controlled by changing γ_{ee}, the onset of fluidity, full hydrodynamic behaviour and ballistics can all be treated equally using this formalism.

II.ii.   Re-formulating the kinetic equation for curved geometries

Here we present our own re-formulation of standard kinetics for a general conformal geometry. This is the tool which will allow the inspection of the effects of geometry upon electrical quantities at the onset of electron fluidity. We begin with a brief discussion of conformal mappings, before outlining our analytic results.

In general, the set of equations

$$u = u(x, y) \qquad v = v(x, y), \quad (2.13)$$

specifies a transformation between the points in the $x - y$ and $u - v$ planes. If each point in the $u - v$ plane corresponds to only a single point in the $x - y$ plane then this is a one-to-one transformation or a mapping. A special case of this occurs when u and v are the real and imaginary parts of a complex analytic function of a complex variable so that

$$f(z) = w = u + iv, \quad (2.14)$$

where $z = x + iy$. Under the condition that $f(z)$ is analytic and $f'(z) \neq 0$ in a region $\mathcal{R}$ then the mapping $w = f(z)$ is conformal at all points of $\mathcal{R}$, meaning that angles are preserved [35]. These mappings have been used extensively to solve a wide range of fluid mechanics and electrostatics problems [35, 36].

Here, conformal maps are used to allow curved geometries to be represented on rectangular computational grids. The application of conformal maps is motivated by the ease of numerical solution on rectangular grids, and the accuracy of the representation of the curved boundary. However this method requires that the kinetic equation (2.1) be reformulated to be solved on geometries described by mappings, so that the electron trajectories we solve for on the rectangular grid represent correctly the electron trajectories on the curved real space geometry.

We shall now consider the effect of the mapping on the conformal geometry, specified by spatial coordinates u and v, where particles may propagate in the directions β. We write the effect of the mapping as a local scale by $C(u, v)$ and rotation by $\alpha(u, v)$ so that some element of the conformal geometry $dw = du + idv$ is related to some element of the real space $dz = dx + idy$ as

$$dz = C(u, v)e^{i\alpha(u,v)} \, dw, \quad (2.15)$$

where it can be noted that $\beta + \alpha = \theta$. Notice that (2.15) is simply equivalent to writing a complex number in polar form. It is important to note that the scaling and rotation factors can be found from the functional form of the mapping, since $dz/dw = C(u, v)\exp[i\alpha(u, v)]$ meaning that $\log(dz/dw) = \log C + i\alpha$. Thus evaluating the derivative dz/dw allows the scaling and rotation factors to be determined.

With this, we have reformulated the kinetic equation in terms of $f = f(u, v, \beta)$, which may then be solved numerically to give the solution for curved current injector geometries located at the boundary. This can be done by realising that taking the modulus of (2.15) gives us the relation between the length of a line element in each geometry

$$(dx^2 + dy^2) = |C(u, v)|^2(du^2 + dv^2), \quad (2.16)$$

which immediately gives us the Lagrangian [37] since

$$\mathcal{L} = \frac{1}{2}m\frac{(d\mathbf{r})^2}{(dt)^2} = \frac{1}{2}m\left(\frac{d\mathbf{r}}{dt}\right)^2, \quad (2.17)$$

where $d\mathbf{r}$ is just the line element of the coordinate system. Thus the Lagrangian is

$$\mathcal{L} = \frac{1}{2}m|C|^2(\dot{\mathbf{u}}^2 + \dot{\mathbf{v}}^2), \qquad (2.18)$$

where $\dot{\mathbf{u}} \equiv du/dt$ and $\dot{\mathbf{v}} \equiv dv/dt$. The usual definitions for finding canonical momenta, P_u and P_v, from the Lagrangian allow the construction of the Hamiltonian

$$P_u = m|C|^2\dot{\mathbf{u}}, \quad P_v = m|C|^2\dot{\mathbf{v}}, \quad \mathcal{H} = \frac{1}{2m|C|^2}(P_u^2 + P_v^2). \qquad (2.19)$$

Then, writing these canonical momenta in terms of the propagation directions to reduce the dimensionality of the problem, as discussed previously, gives the following relations

$$P_u = C\sqrt{2m\varepsilon}\cos\beta, \qquad P_v = C\sqrt{2m\varepsilon}\sin\beta, \qquad (2.20)$$

which may be inverted to to give propagation direction as a function of momentum

$$\beta = \arctan\left(\frac{P_v}{P_u}\right), \qquad (2.21)$$

allowing derivatives with respect to momentum in (2.1)

$$\frac{\partial f}{\partial P_u} = \frac{\partial f}{\partial \beta}\frac{\partial \beta}{\partial P_u}, \qquad \frac{\partial f}{\partial P_v} = \frac{\partial f}{\partial \beta}\frac{\partial \beta}{\partial P_v}, \qquad (2.22)$$

to be replaced with derivatives with respect to β

$$\frac{\partial \beta}{\partial P_u} = -\frac{P_v}{P_u^2 + P_v^2}, \qquad \frac{\partial \beta}{\partial P_v} = \frac{P_u}{P_u^2 + P_v^2}. \qquad (2.23)$$

To put all of this together, we use the Poisson bracket [37] relation

$$\frac{\mathrm{d}f}{\mathrm{d}t} = \frac{\partial f}{\partial t} + [f, \mathcal{H}], \qquad (2.24)$$

where $\mathcal{I}[f] \equiv df/dt$, to write the full kinetic equation for this problem

$$\mathcal{I}[f] = \frac{\partial f}{\partial t} + \frac{v_F}{C}\left[(\mathbf{v}\cdot\nabla f) - \frac{\partial f}{\partial \beta}(\mathbf{v}\cdot\nabla\alpha)\right], \qquad (2.25)$$

where v_F is the magnitude of the Fermi velocity. We see that the conformal map introduces scaling by $1/C(u,v)$ and a term proportional to $\nabla\alpha(u,v)$ which rotates particle trajectories. This must now be solved for $f = f(u,v,\beta)$, with appropriate boundary conditions, then (2.6) and (2.7) can be applied to study the onset of fluidity on curved geometries and reveal how both geometry and ℓ_{ee} impact measurable electrical quantities like potential and current.

While our analytic result is totally general, we focus on solving two geometries. First, a half-ellipse (needle) current injector at the edge of a sample. Such a geometry is of interest experimentally, since it might allow the
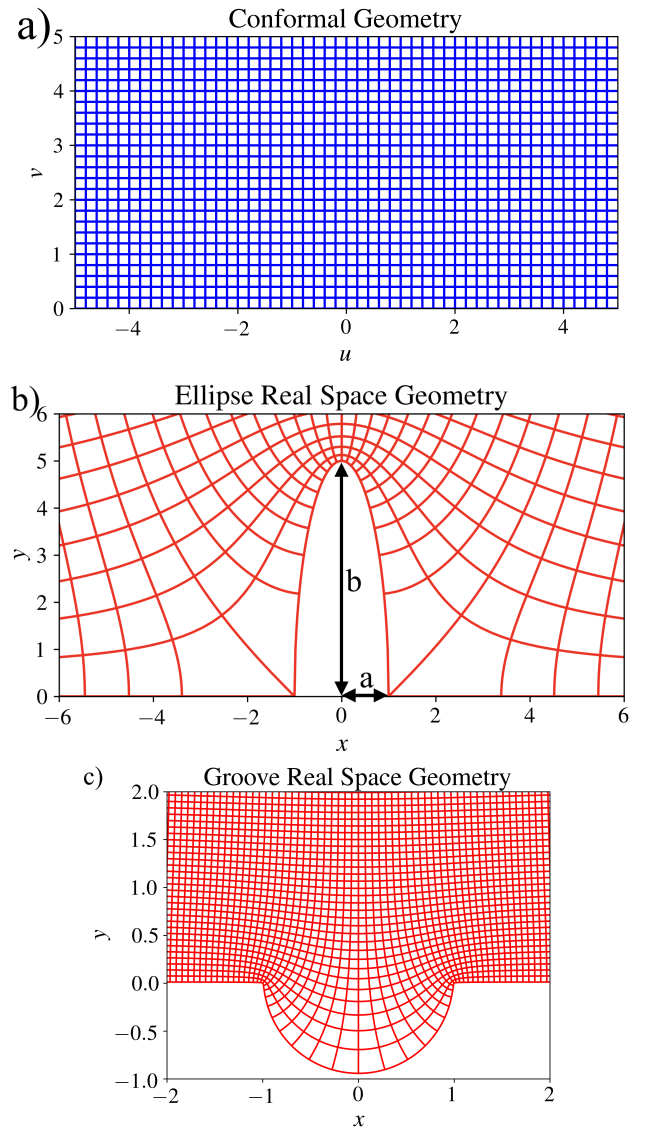

FIG. 1: Effect of mapping a) upper half plane to geometries with curved boundaries: b) a half-ellipse and c) a semi-circular groove. The map to the elliptic boundary is given by (2.26) with semi-minor axis a and semi-major axis b. The semi-circular groove mapping is given by (2.27).

predicted fluidic implications [26] of elliptic geometries to be realised in clean nanoscale material samples. The half-ellipse geometry is described by the mapping [38] from the upper half plane described by $w(u,v)$ using the complex analytic function

$$z = aw + b\sqrt{w^2 - 1}, \qquad (2.26)$$

where $z = x + iy$ and $w = u + iv$, with a and b the semi-minor and semi-major axes of the ellipse, respectively. The application of this mapping is shown in FIG. 1.

We also consider a semi-circular "groove" geometry,

given by the mapping

$$z = \frac{(w+1)^{3/2} + (w-1)^{3/2}}{(w+1)^{3/2} - (w-1)^{3/2}}, \qquad (2.27)$$

where z and w have the same meanings as before, and the effect of the mapping is shown in FIG. 1. When discussing the half-ellipse geometry we have the freedom to change a and b to investigate how this changes the physical response of the system. For convenience, we express these degrees of freedom as the single parameter, curvature radius R_c, defined as

$$R_c = \frac{a^2}{b}. \qquad (2.28)$$

For our investigations we fix $a = 1$ and change b. The mapping for the "groove" does not have these additional parameters to investigate.

II.iii.　Boundary Conditions

In order to solve (2.25), suitable boundary conditions must be applied. The boundary conditions used are shown in FIG. 2, here we shall briefly discuss the assumptions behind them.

We assume that all boundaries other than the $y = 0$ boundary and the ellipse are absorbing. In other words, outside of the domain we study, electrons move freely into the background sea of electrons. The current injecting ellipse is endowed with a uniform current density and is normalised to inject unit current, so that

$$\iint J(\mathbf{r}, \beta) \sin \beta \frac{d\beta}{2\pi} dx = 1. \qquad (2.29)$$

This is arguably an over-simplification since in experiment it is a uniform potential that is applied, however this would add an additional level of complexity, since current density must then be treated as unknown, (i.e. see [27]). While simple, this model provides a good first step in understanding this regime on curved geometries. The angular distribution of the source gives a useful way of tuning the strength of contact resistance. Here, the larger the difference between the angular distribution of injected current and the angular distribution of the bulk solution, the larger than contact resistance.

We also impose that the current injecting ellipse and lower boundary $y = 0$ scatter perfectly diffusively according to Lambert's law [39]. In other words, as well as the injected current, the boundary behaves as an isotropic current source due to this scattering. This condition is expressed by conserving flux at the boundary

$$f_s(u, v = 0, \beta > 0) = \frac{1}{2} \int_0^\pi \sin \beta' f(u, v = 0, -\beta') d\beta', \qquad (2.30)$$

so that upwards flux is equal to downwards flux. The factor $1/2$ comes from integrating $\sin \beta$ between 0 and π,
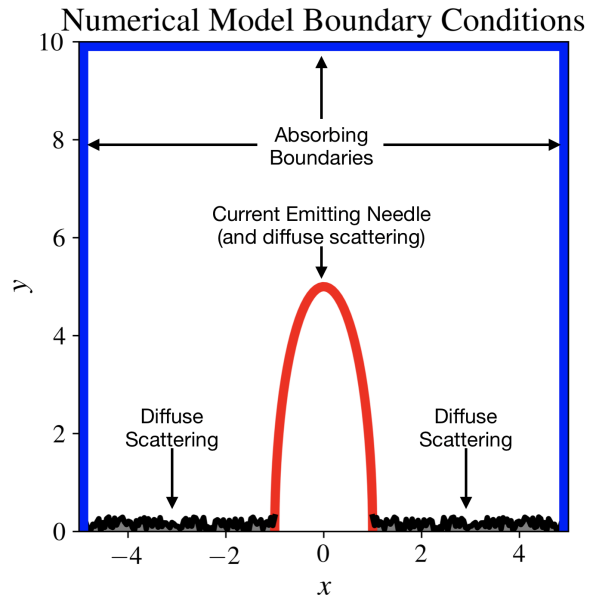

FIG. 2: Boundary conditions applied to the numerical model. All boundaries other than the emitting boundary and the $y = 0$ boundary are perfectly absorbing (shown as blue). The lower boundary and current injector scatters perfectly diffusively, according to (2.30) (shown as grey/black rough surface). A uniform current density is applied to the current injecting region (red), defined through (2.29).

providing a normalisation factor. This condition means that, rather than being lost, downwards moving particles are exactly compensated by the boundary condition, being re-emitted equally in all directions. Once again, this is the simplest possible model for boundary scattering, however this provides a well understood way of describing the boundary and has been used to solve similar problems [26].

III.　Numerical Solution of the Kinetic Equation

The reformulated kinetic equation (2.25) has been solved numerically, with the boundary conditions specified in Section II iii. In this section, the methods of numerical solution are outlined and justified, with the difficulties presented by curved geometries and methods of handling these also being mentioned. The two most important validations that were performed are presented in detail, with several of the other validations mentioned.

We begin by re-writing (2.25) as

$$\frac{\partial f}{\partial t} = \mathcal{I}[f] - \frac{1}{C}\left[(\mathbf{v}\cdot\nabla f) - \frac{\partial f}{\partial\beta}(\mathbf{v}\cdot\nabla\alpha)\right]$$
$$+ J(\mathbf{r},\beta) + f_s(u, v = 0, \beta > 0), \quad (3.1)$$

where we define the right hand side as the residual, $r = r(u, v, \beta)$. The terms describing the injected current distribution $J(\mathbf{r}, \beta)$ and the effective secondary source due to boundary scattering, f_s have also been included. Then the time derivative on the left hand side has been approximated as

$$\frac{\partial f}{\partial t} \approx \frac{f^{t+\tau} - f^t}{\tau} \Rightarrow f^{t+\tau} = \tau r + f^t \qquad (3.2)$$

where f^t denotes the distribution function $f(u, v, \beta)$ at time t, and τ is the time step. Moving to a discrete representation of the problem, functional dependences are replaced with indexes of the arrays used to represent r, f etc. Therefore $f(u, v, \beta) \rightarrow f_{ijk}$, where i labels the u grid, j the v grid and k the discretised propagation direction grid, β. Since we are only interested in steady state solutions, we iteratively step through time until the change of f with time, given by the residual, is sufficiently small.
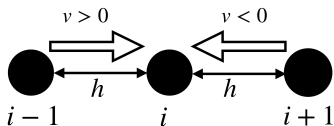

FIG. 3: Schematic representation of the upwind finite difference scheme. The distribution at i is determined by moving the distribution at point $i \pm 1$ onto point i, depending upon the direction of the particle velocity. This scheme is well known to be stable (under the well known CFL condition) and produce accurate transport properties [40].

Two main approaches have been used to represent (2.25) on discrete spatial and directional grids. The collision integral (2.10), $\partial/\partial\beta$, and scattering boundary condition (2.30) have been expressed a operator matrices, so that taking the dot product between the matrix f_{ijk} and the operator matrix represents the corresponding term in the kinetic equation. The $\mathbf{v}\cdot\nabla\alpha$ term does not change with time, so can be pre-calculated to just provide a prefactor for $\partial f/\partial\beta$. With this, we need only discretise what is just the advection equation $\partial f/\partial t = -\mathbf{v}\cdot\nabla f$. For this type of advection problem it is common [40] to use upwind finite differences, shown schematically in FIG. 3. This scheme, in one dimension, is written as

$$\frac{f_i^{t+\tau} - f_i^t}{\tau} = -v_i^t \begin{cases} \frac{f_i^t - f_{i-1}^t}{h}, & \text{for } v > 0 \\ \frac{f_{i+1}^t - f_i^t}{h}, & \text{for } v < 0 \end{cases} \qquad (3.3)$$

where h is the grid spacing, as in FIG. 3. The fidelity of the transport described by this scheme may be under-

stood by considering the flow of information in the physical system. If a particle is moving to the right $v > 0$, then the distribution at the point i depends upon the point $i - 1$, as this is the part of the distribution that is being "blown" along the chain of grid nodes. The opposite is true if the particle is moving to the left, $v < 0$: the distribution at point $i + 1$ is being "blown" onto grid point i. This scheme is both stable, and produces the correct transport properties [40]. It is also straightforward to extend this to two dimensions.

Some care must be applied when utilising these finite difference schemes on the curved geometries, since FIG. 1 shows how grid squares on the conformal geometry are stretched by the factor $C(u, v)$, meaning that the grid step on the conformal geometry, $\Delta u, \Delta v$, must be small enough to produce sufficiently accurate results on the real space grids, where the grid steps are $\Delta x = C\Delta u\cos\alpha - C\Delta v\sin\alpha$ and $\Delta y = C\Delta v\cos\alpha + C\Delta u\sin\alpha$, meaning that the grid steps in real space are larger than on the computational grid. Additional difficulty is presented by the half-ellipse mapping (2.26), due to the square root singularity at $w = \pm 1$. Indeed, the function is no longer complex analytic at these points, so does not provide a conformal map here. This has been avoided by shifting our domain a small distance away from the singularities, by saying $w_\kappa = w + \kappa i$, where κ is the smallest number for which the numerical scheme will converge to a solution within a reasonable time.

Several important validations have been performed upon the numerical model, to verify that results are physically consistent. One of the most important validations performed was the check that current is conserved. Let us consider a Gaussian current source centred at (u_0, v_0) with standard deviation σ

$$J(\mathbf{r}, \beta) = A\exp\left(-\frac{1}{2\sigma^2}\left[(u - u_0)^2 + (v - v_0)^2\right]\right), \tag{3.4}$$

where the coefficient A is determined by normalisation, placed in the centre of a rectangle, where all four boundaries are absorbing. In two dimensions, current conservation requires that

$$\mathbf{J}(\mathbf{r}) = ne\mathbf{v}(\mathbf{r}) = \frac{I}{2\pi r}\hat{\mathbf{r}}, \tag{3.5}$$

where I is the total injected current. Verifying correct current conservation is extremely important, since a failure to do this means that transport is not represented correctly, leading to unphysical results which cannot be meaningfully interpreted. The result of this validation is shown in FIG. 4. We plot $J(r) \times 2\pi r = I$, which should be normalised to be 1, so that the plot one should expect for a correctly behaving model would be a constant $y = I = 1$ line. This allows us to verify both the correct $1/r$ behaviour and the conservation of current, given by the factor 2π in two dimensions. We demonstrate that current is successfully conserved to within $\sim 10^{-3}\%$. This verifies the correct representation of
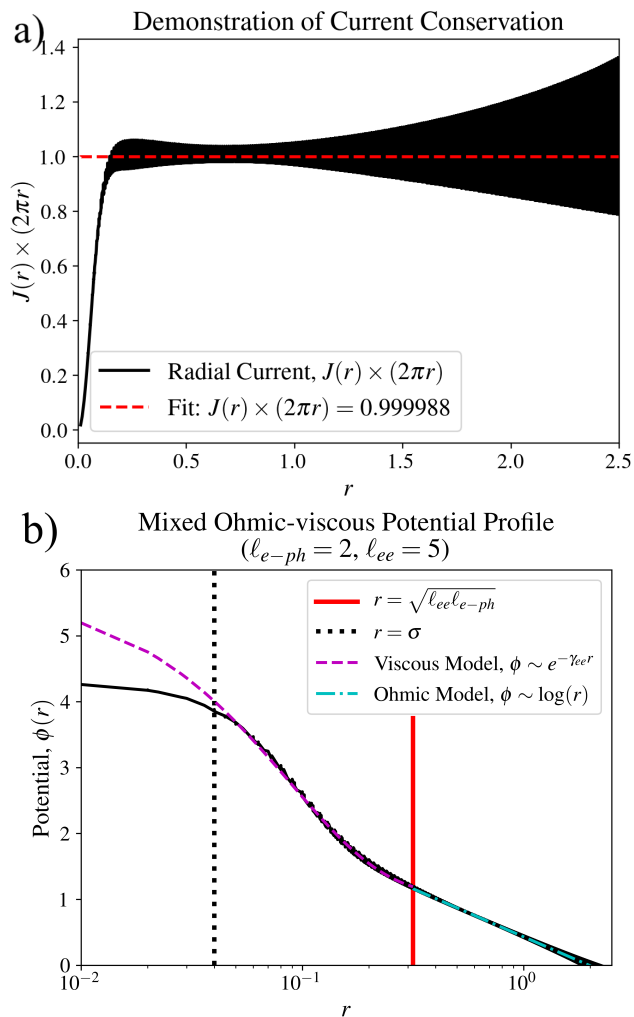
FIG. 4: Validations of the numerical model: a) demonstrates current conservation to within $\sim 10^{-3}\%$, as well as the expected $1/r$ decay. b) shows our validation of the theory presented in [10], demonstrating correct mixed Ohmic-viscous described by (1.1) at the correct quantitative length scales, solved using our kinetic framework.

transport properties (since physical quantities are conserved) and correct normalisation (we aim to inject unit current, and this is what is demonstrated). The large oscillations around the average seen in FIG. 4 are artefacts of constructing a circle at radius r on a grid made from rectangles. Behaviour at small r is distorted by the finite size, σ, of the Gaussian source.

Another important validation performed was a demonstration of mixed Ohmic-viscous behaviour [10]. Described by the Ohm-Stokes equation (1.1), the situation where a single sample can exhibit both Ohmic and viscous flow patterns has been experimentally realised [12, 23]. In graphene, the Ohmic terms are weak, meaning that at short distances exponential suppression of the potential is expected, $\phi \propto e^{-r/\ell_{ee}}$, corresponding to vis-

cous flow. Then at distances $\xi = \sqrt{\ell_{e-ph}\ell_{ee}}$ [10] the Ohmic contribution becomes dominant, giving $\phi \propto \log(r)$ behaviour. In FIG. 4 we demonstrate the excellent verification of this behaviour. At distances $r < \sigma$, the finite size of the Gaussian source distorts behaviour, however for $\sigma < r < \xi$ least squares fitting of the expected viscous model shows excellent agreement with our solution. Then at distances $r > \xi$ least squares fitting demonstrates the correct Ohmic behaviour. This validation shows that our model re-creates important literature results correctly, giving both the correct crossover point, ξ, as well as the correct Ohmic or viscous behaviour at the corresponding length scales. This highlights the advantages of using a fully kinetic description: we can access both fluid mechanics, ballistics and Ohmic behaviour on equal footing by simply changing parameters of the model.

It is important to note that several other validations were performed, but are not discussed in detail here. For example, as well as the mixed behaviour shown in FIG. 4, Ohmic and viscous behaviour were also validated in isolation. The scattering boundary condition was validated by recreating the space charge results for a point source on the boundary given in [10]. The correct application of the bending terms in (2.25) was validated by checking that particles propagate in straight lines on the real space grid in the ballistic limit. With all key elements thoroughly validated we now present our results.

IV. Results and Discussion

We present the results of solving (2.25) using the boundary conditions given in Section II iii and the numerical methods outlined in Section III. Electrical potentials and distances are given in arbitrary units. Here, we shall answer the questions posed in Section I: are hydrodynamic effects observed at the onset of fluidity? How do these depend upon R_c and ℓ_{ee}? When are they maximal? These will be answered first for the half-ellipse geometry and then the groove geometry. Since we are interested in viscous effects, we set $\gamma_{e-ph} = 0$ (i.e. $\ell_{e-ph} = \infty$ so electrons never scatter inelastically).

Potential maps for the half-ellipse geometry with $R_c = 1/5$ are shown in FIG. 5. The large suppression of potential at the tip of the needle predicted by solution of the Stokes equation [27] but we see here that it is also observed in the crossover regime. The effect is observed in the crossover regime both with minimal contact resistance, *and* with large contact resistance. This prediction is critical if this effect is to be observed experimentally. The origin of the negative response here can be understood by noting that the current changes sign quickly over the needle tip. This requires electrons to be backscattered, moving against the applied potential, resulting in a "windshear" effect caused by the current changing sign. We demonstrate that the viscous effects, predicted by hydrodynamic theory [27], are also observed
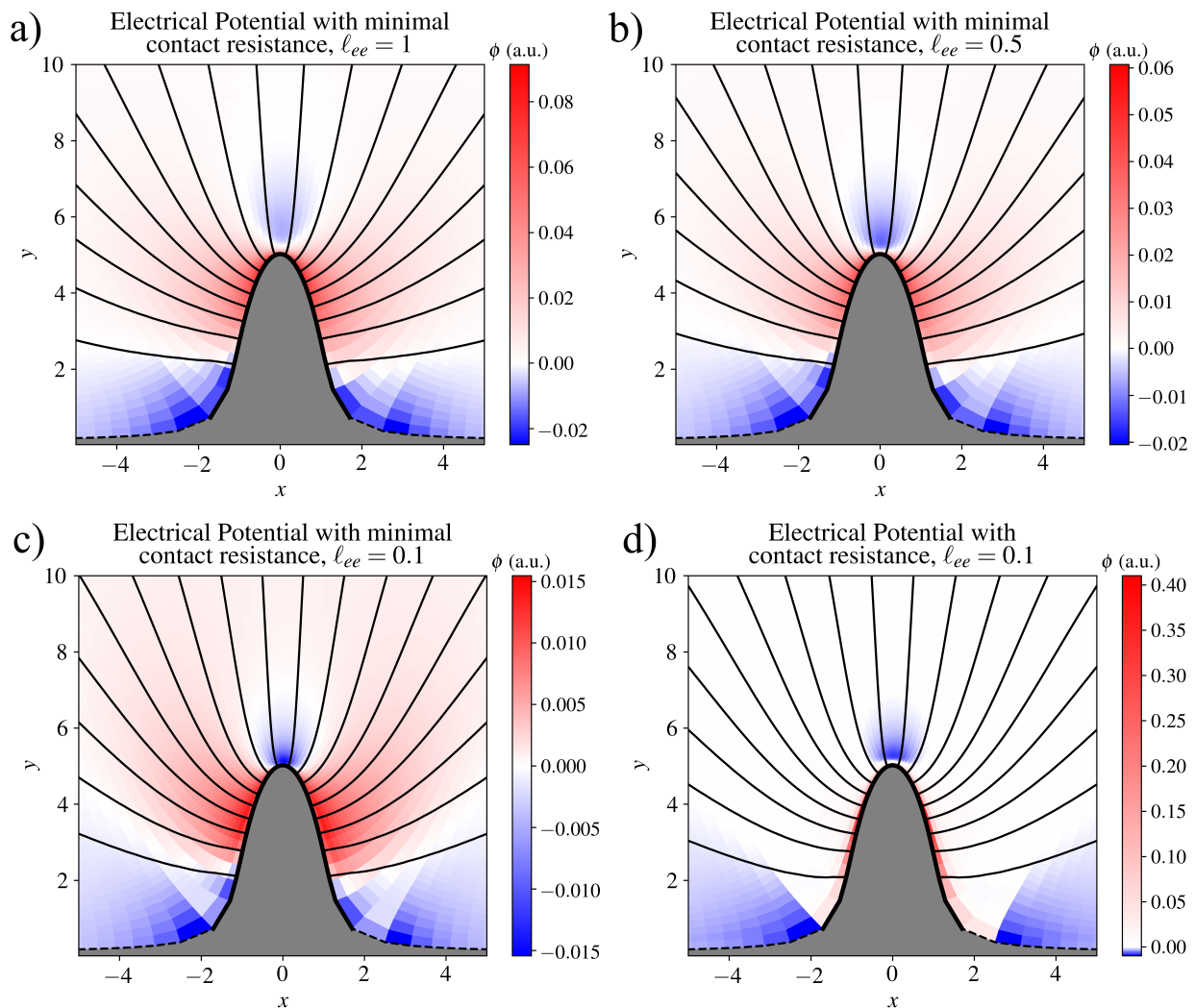
FIG. 5: Potential maps for the half-ellipse current injector, with $R_c = 1/5$. Unit current is injected through the thick black line along the boundary and black lines are streamlines, indicating electron flow directions. a), b) and c) have minimal contact resistances, while d) has large contact resistance.

at the very onset of fluidity. In addition, FIG. 5 qualitatively hints at how the negative response depends upon ℓ_{ee}: a smaller mean free path enhances the suppression. Examining colour bar values in FIG. 5, we see that for $\ell_{ee} = 1$ the negative response is $\sim 20\%$ the strength of the signal, but for $\ell_{ee} = 0.1$ the negative response is roughly as strong as the signal. This qualitative understanding gives us a good idea of what to expect when the full dependence upon ℓ_{ee} is characterised. To better understand the behaviour, the potential profile in a vertical line from the tip of the needle is shown in FIG. 6 for various mean free paths both with and without contact resistance. This shows clearly that for minimal contact resistance, decreasing ℓ_{ee} produces larger suppression and that this is greatly reduced but still present for large contact resistance. The reduction of this effect by contact resistance can be understood by remembering that $V = IR_V$ (where R_V is contact resistance). A

larger contact resistance produces a larger electrode voltage in order to drive the same current (which is fixed by the boundary condition), as can be seen by noting the scales of the potential colour maps in FIG. 5. This means that if the effect producing the negative response is truly caused by the curvature at the needle tip then it's strength remains basically unchanged in the presence of contact resistance. As a result, the geometric curvature drives the same backflow, which is now much smaller when compared to the applied potential. The effect becoming small compared to the background makes it difficult to observe, presenting an experimental challenge in minimising contact resistance to observe this effect. This is indeed what is demonstrated in FIG. 5 and FIG. 6.

In addition to the potential drop at the tip of the needle, which is the effect of interest, FIG. 5 exhibits large potential drops at either side of the needle. These arise from a similar "windshear" effect as at the tip of the nee-
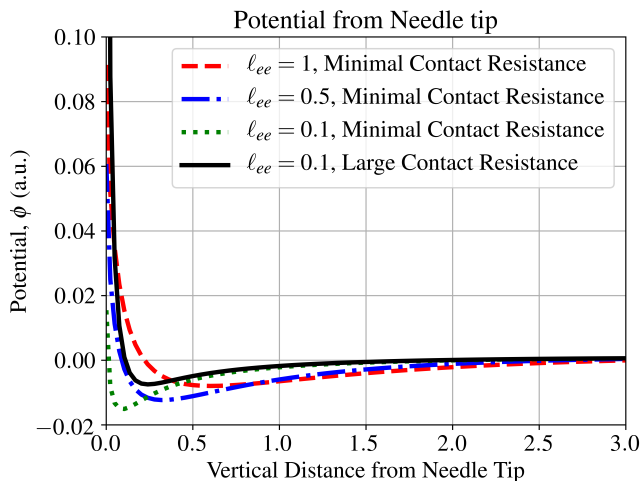
FIG. 6: Vertical potential profiles from the needle tip, for minimal contact resistance for several ℓ_{ee} and for large contact resistance, corresponding to the potential maps shown in FIG. 5. For minimal contact resistance, suppression grows with ℓ_{ee} and viscous suppression is also seen in the presence of contact resistance, although the effect is significantly weaker.

FIG. 7: The effect of ℓ_{ee} and R_c upon the potential at a) the very tip of the needle and upon b) the smallest value of potential. Behaviour of the minimal value of potential as $\ell_{ee} \to 0$ is shown in b), inset.

dle, however they are located near the square root singularity of the mapping (2.26), meaning that C is very large here, causing significant deformation of the grid. Therefore the discretisation here is poor, so the numerical scheme will not produce a sufficiently accurate solution here. The illustration of the mapping in FIG. 1 shows how the grid squares are stretched significantly at the singularity points, but not at the tip. Hence why our solution and discussion of the behaviour at the tip is valid, but conclusions are not drawn about the regions either side of the needle.

Next, the effect of curvature radius and ℓ_{ee} upon the potential at the very tip of the needle, and the minimal value of potential was considered. These results are given in FIG. 7. It can be seen that the potential at the tip of the needle is always positive. This means that the negative region observed in FIG. 5 forms some finite distance away from the needle tip. This is consistent with the fact that a uniform current density is enforced as a boundary condition for the model. If one were to instead apply a uniform potential then one might expect the negative region to sit directly upon the tip, as for the fully fluid mechanical treatment [27]. The potential at the tip is suppressed as one decreases ℓ_{ee}, and at the same time the potential is increasingly suppressed as curvature radius decreases. The increase in suppression with decreasing curvature radius, over all ℓ_{ee} is consistent with the origin of the negative response being the shearing of fluid at the tip. A smaller curvature radius means that the direction of current changes more quickly, producing larger viscous shear at the tip of the needle resulting in greater backflow. The suppression then becomes larger as ℓ_{ee} is
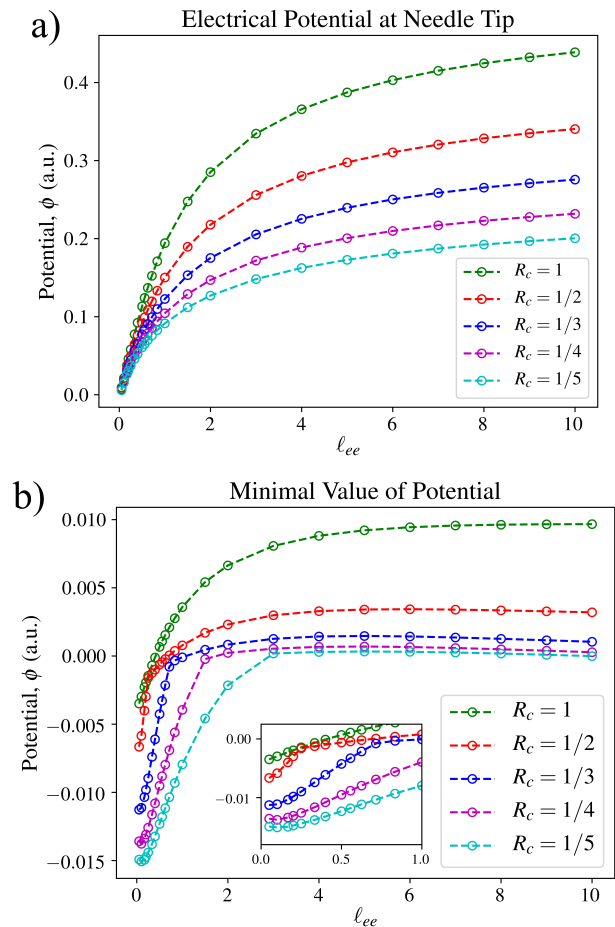
decreased. Since the effect of the geometric curvature upon the flow is mediated by electron-electron collisions, the more frequently these occur the more strongly the effect of shearing is felt by the fluid. This is key to understanding the behaviour of the minimal value of potential, shown in FIG. 7. Once again, it can be seen that geometric curvature (enhanced by reducing R_c) produces a voltage suppression due to shear at the tip which is enhanced further by reducing ℓ_{ee}. It should be noted that for a semi-circular boundary, $R_c = 1$, a negative voltage is only produced for very small ℓ_{ee} however negative voltages are accessed more easily as curvature radius is made smaller. The behaviour at small ℓ_{ee} remains inconclusive. One might expect this this to saturate at a constant value dictated by R_V, or to increase again as $\ell_{ee} \to 0$, as a fully fluid mechanical treatment predicts [26]. The results presented here might indicate either behaviour, and finer grids could be used to answer this question. The hydrodynamic limit is difficult to reach since capturing flow behaviour accurately requires that $\Delta x, \Delta y < \ell_{ee}$ (i.e. we require several grid nodes per

a) Electrical Potential in the Ballistic Limit
$\ell_{ee} = 100$

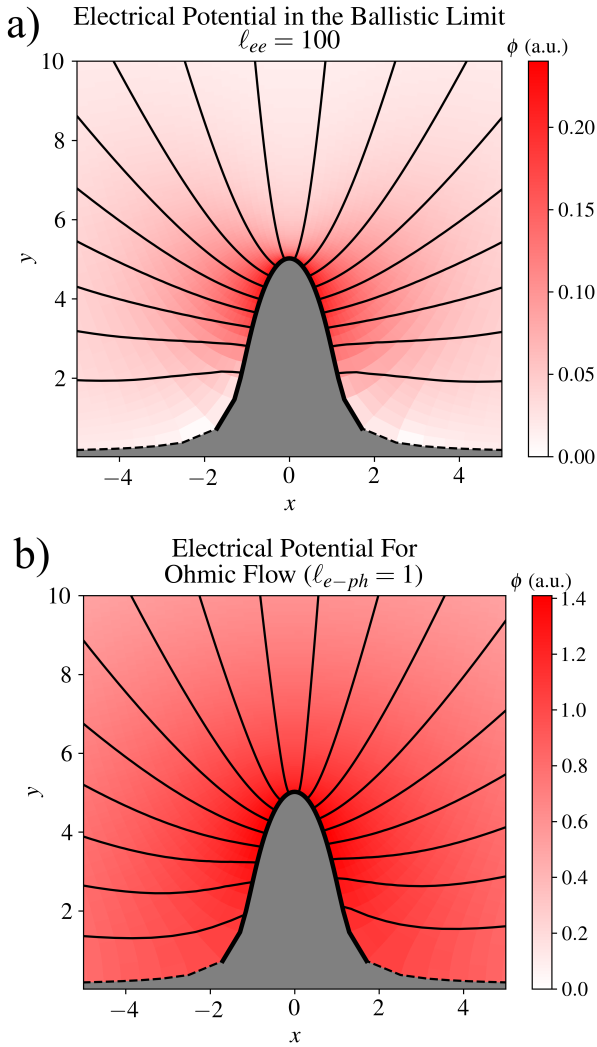## b) Electrical Potential For Ohmic Flow ($\ell_{e-ph} = 1$)

FIG. 8: a) Ballistic and b) Ohmic flow patterns for the needle current injector. In both cases no potential suppression at the tip is observed, demonstrating that this effect is a direct consequence of elastic electron-electron interactions.

mean free path to properly approximate the behaviour), and finer grids require significantly more computational work.

What we witness here, shown in FIG. 5, FIG. 6 and FIG. 7, is an effect which arises from electron-electron interactions, in a regime which is *not* fully hydrodynamic. We can demonstrate that this is indeed the effect of electron-electron interactions by contrasting the behaviour with the ballistic limit and Ohmic transport, both of which are easily accessible using the kinetic treatment. The flow patterns for these regimes are shown in FIG. 8. We see that in both Ohmic ($\ell_{e-ph} < \ell_{ee}, L$) and ballistic ($L < \ell_{ee}, \ell_{e-ph}$) regimes, where electron-electron interactions are not the dominant transport mechanism, there is no suppression of potential at the tip of the needle. This demonstrates that electrons moving against

the potential is indeed due to collective motion arising from elastic electron-electron scattering. It is, however, unclear whether this effect is maximal at the crossover from ballistics to hydrodynamics, as is predicted for simpler geometries [26], which is a question that might be answered by the behaviour at smaller mean free paths. Regardless of this, we show that the fingerprints of electron viscosity, arising from elastic electron-electron collisions, are observed in the crossover regime, and that these effects can enhanced by choosing geometries which induce a larger shearing force on the fluid.
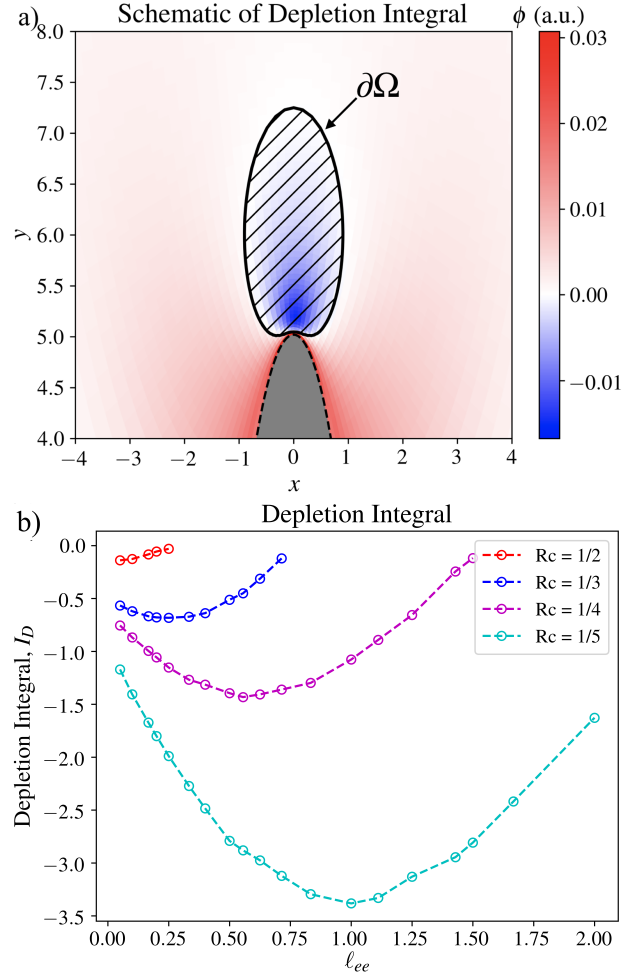
a) Schematic of Depletion Integral

b) Depletion Integral

FIG. 9: a) Schematic representation of the depletion integral (4.1), b) the variation of this quantity with ℓ_{ee} and R_c. Only results where the negative region was present have been included. In contrast to FIG. 6 and FIG. 7, these results exhibit a clear minima at intermediate mean free paths.

So far, it seems as though if one wanted to observe this effect experimentally then the smallest possible curvature radius of the half-ellipse should be used, along with a minimal ℓ_{ee}. However another characteristic of the crossover regime which is of interest is the amount of depletion the backflow causes. Knowledge of such
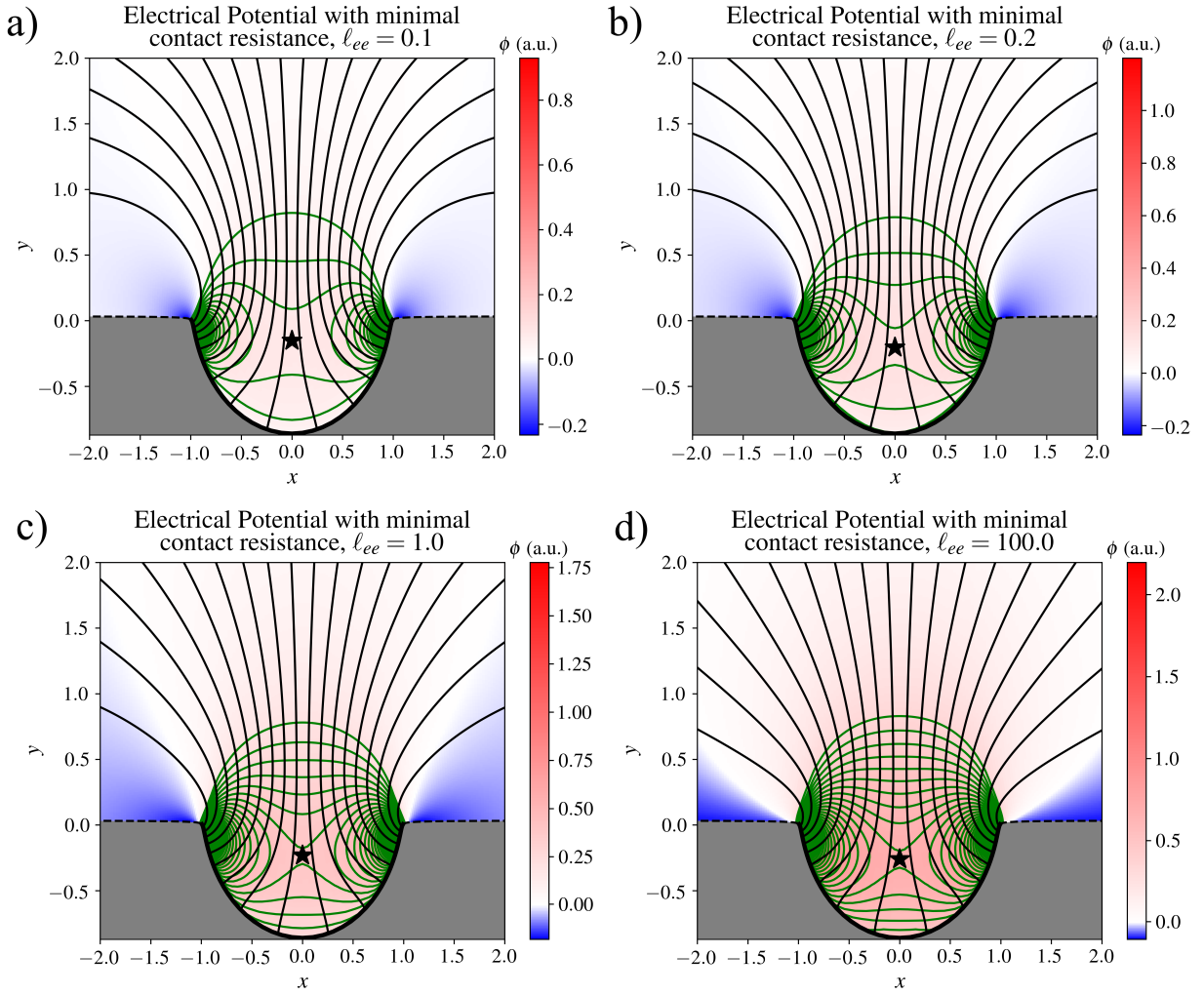
FIG. 10: Potential maps for the groove geometry. Unit current is injected through the solid black line along the curved boundary. Black lines are streamlines and denote the trajectories of electrons. Green lines are potential isolines, shown in the vicinity of the groove to illustrate the build up of charge inside the cavity. Stars indicate the position of maximal potential inside the cavity, caused by collective motion of electrons. Maps a), b) and c) demonstrate the presence of the effect at the crossover from ballistics to hydrodynamics and d) shows that the effect is also present in the fully ballistic regime.

behaviour is of obvious interest for scanning gate microscopy methods for imaging the electron flows [28, 29]. Since these methods use a needle to image flows, our results indicate that these methods cause depletion of the electron fluid. A natural question to ask might be: under what conditions is the depletion maximal? To answer this question, we define the depletion integral as

$$I_D = \int_{\partial\Omega} \phi(x,y)dxdy, \qquad (4.1)$$

where the region $\partial\Omega$ denotes the entire negative region formed at the tip. This is obtained by drawing contour lines of the potential and then defining the region $\partial\Omega$ as the area inside the zero potential contour drawn around the region of negative potential at the tip (shown in FIG. 9). The potential is then integrated over this

region. The dependence of I_D upon ℓ_{ee} and curvature radius is presented in FIG. 9. Only data where the zero potential contour could be drawn have been included in FIG. 9. If one only considers the potential the tip, then FIG. 7 indicates that a minimal mean free path should be used in order to observe the effect most strongly, however FIG. 9 shows that values of the depletion integral exhibit clear minima at intermediate mean free paths. Again we see that since this effect is due to shear at the tip of the needle, the depletion is larger for smaller curvature radii and the effect is only accessible for increasing mean free paths as curvature radii is increased. This means that the collective motion of electrons, driven by their interaction, is demonstrated to be maximal for an intermediate value of ℓ_{ee}, which depends upon exact geometry.

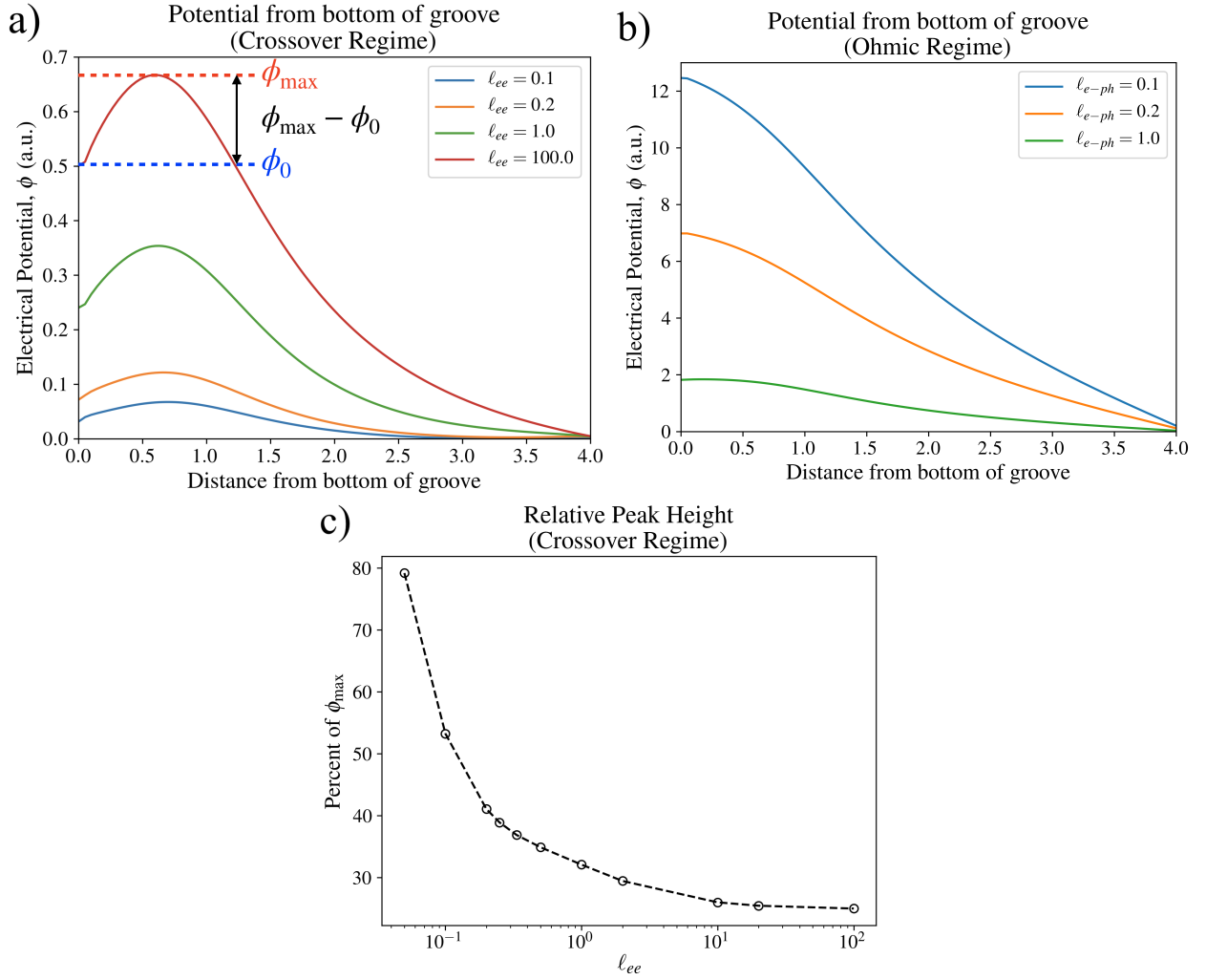This leads us to conclude that for the needle geome-

FIG. 11: Potential profile from the bottom of the groove for several ℓ_{ee} shown for a) the crossover from ballistic to hydrodynamic flow and b) Ohmic flow. The location of the peak is shown as a star on the colour maps in FIG. 10. The vanishing of the effect when moving to Ohmic flow demonstrates that this is an interaction driven effect. c) Relative height of the peaks shown in a) to show that if one considers the relative height, the viscous boost is increased as ℓ_{ee} is decreased.

try, the effects of viscosity are pronounced by geometric curvature, thus as small as possible R_C should be used to observe this effect. Then, to maximise the chances of detection using only potential measurements a minimal ℓ_{ee} should be used, however if one can measure depletion or the size of the negative region then intermediate mean free paths are preferable. It could also be useful to connect the length scales at which the negative response is maximal to features of the geometry, for example it has been suggested [27] that the negative response might be maximal when $\ell_{ee} \sim a$ (where a is the semi-minor axis of the ellipse). While our results for depletion integral in FIG. 9 hint at this kind of behaviour, a detailed analysis of this is beyond the scope of this work.

In addition to the needle geometry, we also consider a groove geometry, shown in FIG. 1. Potential maps for this geometry are shown in FIG. 10. If one solves this problem in the low Reynolds number hydrodynamic limit, using the Stokes equation, i.e. (1.1) with $\rho = 0$, then viscous effects are expected to lead to a build up of charge somewhere inside the cavity. This can be thought of as the exactly opposite effect to the depletion that is seen for a needle current injector. The positive contribution can be understood by examining the streamlines in FIG. 10. On the needle geometry, the streamlines clearly show the shear at the tip of the needle as they are "splayed", and here they are "pushed" together. Then, the equipotential lines (shown in green in FIG. 10) show that electrons are flowing against the potential to collect at the maximal point. This means that the regions around the maximal value (shown as a star in FIG. 10) are depleted, as for the needle geometry, in order to support the collection of charge at the maximal value. This is demonstrated if one considers the profile of potential

from the bottom of the groove, moving vertically upwards, shown in FIG. 11. We see clearly the effect of viscous backflow upon producing a well defined maxima of potential inside the groove. For larger ℓ_{ee} the peak is larger, which might lead to the conclusion that the effect is maximal as one moves towards the ballistic regime. However, it makes more sense to instead consider the relative size of the peak by looking at the quantity $100\times(\phi_{\max}-\phi_0)/\phi_{\max}$, where $\phi_{\max}$ is the peak value, and ϕ_0 is the potential at the bottom of the groove (shown on FIG. 11). This is plotted in FIG. 11, and gives the height of the peak as a percentage of the maximal value of the peak. Looking at the relative height allows the size of the effect relative to the background to be shown, which is a more important consideration for experimental validation. We see that by considering the relative height of the peak instead of its absolute value, the potential boost is larger for smaller ℓ_{ee}. This is consistent with our expectation that this effect is caused by the geometric curvature but mediated by elastic carrier collisions, resulting in a viscous response at the onset of fluidity. Interestingly, unlike the needle geometry the effect is visibly present in the ballistic regime, however is still washed away in the Ohmic regime, as we see in FIG. 11. We see that for Ohmic flow there is no longer a build up of charge inside the cavity demonstrating that, as for the suppression of potential at the tip of the needle, this effect arises directly due to carrier interactions.

Our results here are inconclusive, however predict the effects of electron-electron interactions to be present in the crossover from hydrodynamic to ballistic flow for this geometry, although it remains unclear whether the effect is enhanced in this regime.

V. Conclusion

To conclude, we have presented our own reformulation of the Boltzmann kinetic equation for a general curved geometry described by a conformal map (2.25), then solved this numerically to investigate the effect of geometric curvature on electron flows at the onset of fluidity. We have extended understanding beyond the onset of fluidity in a Hall Bar geometry [26] and curved geometries in a fully hydrodynamic limit [27]. The questions we aimed to answer were: are the fully hydrodynamic effects predicted by (1.1) also present at the onset of fluidity? How do these depend upon parameters of the geometry and ℓ_{ee}? When can these effects be maximally observed? To answer these questions we considered both a half-ellipse current injector and a semi-circular groove current injector, investigating how current injector curvature plays a role in determining potential and flow patterns.

For the needle current injector, hydrodynamic theory predicts a large voltage suppression at the tip of the needle and for the groove current injector a charge build up inside the cavity is predicted. We demonstrate that both of these effects are observed in the crossover from ballistics to hydrodynamics, at the onset of fluidity. By contrasting our results at the onset of fluidity with results for Ohmic flow we show that both the voltage suppression and the voltage boost are direct consequences of carrier interactions, meaning that we observe effects that are understood in terms of viscous fluids, at the very onset of the hydrodynamic regime. Since we have shown that the effects of viscosity are seen both with minimal and large contact resistance, there is cause for optimism that these effects could be experimentally realised.

We have shown that these effects are sensitive to both ℓ_{ee} and curvature effects. For the half-ellipse current injector, a smaller curvature radius produces a larger voltage suppression at the tip. This arises because a smaller curvature radius produces a larger shear at the tip, and since viscosity is the resistance to shear, the voltage suppression due to this becomes larger. Electrons flow *against* the potential to compensate the change in sign of the current. The de-coupling of current and potential distributions characteristic of carrier interaction dominated transport regimes [9, 26] is shown to be present at the onset of fluidity and caused by geometric effects. We find that then decreasing ℓ_{ee} further increases the voltage suppression, indicative of a carrier interaction dominated transport regime. Similarly for the groove geometry, we demonstrate that curvature produces flow against the potential due to collective motion of electrons, at the onset of fluidity. Instead of producing a suppression of potential a "boost" is observed, whereby charge builds up at a maximal point inside the cavity. We find that again this is sensitive to ℓ_{ee} and that if one considered the relative height of the potential peak, then the effect becomes more pronounced at smaller mean free paths. Again this is the observation of a carrier interaction dominated regime, at the onset of fluidity.

The viscous suppression or boosting of potential is shown to be maximal for small ℓ_{ee}, although there are hints that the effects could be maximal for intermediate mean free paths. So, to observe this effect maximally, one should use as small as possible mean free path and curvature radius. Although behaviour as $\ell_{ee} \to 0$ remains inconclusive, this could be examined using this model.

We leave several open questions that could be investigated using this model. A more complete study of the effect in the presence of contact resistance and at smaller mean free paths would be useful for experimental realisation of this, or in connecting this theory to experimental results and other studies in the fully hydrodynamic limit. Also, more realistic boundary conditions could be applied. A uniform current density is not experimentally practical, so instead a uniform potential should be used. Aside from simple extensions of this work, our model could be used to answer several deeper questions. For example, weak magnetic fields can be used to image electron flows [28], so the effects of these should be considered. This is an almost trivial extension to this model, since we have already expressed $\partial/\partial\beta$ as

an operator matrix, and an external magnetic field simply adds a $\omega_c \partial f/\partial \beta$ term to the kinetic equation, where $\omega_c = eB/m$ is the cyclotron frequency. This would allow the intrusiveness of such measurement methods upon electron flows to be considered in full detail for a wide range of mean free paths. Additionally, since our analytic results are completely general, many other current injector shapes could be investigated, including variously shaped cavities and steps etc. A detailed analysis of the length scales at which the effects of interactions are dominant would also be of interest. For example, is the distance at which the negative response is largest dependent upon a, b or R_c?

[1] M. J. M. Jong and L. W. Molenkamp. Hydrodynamic electron flow in high mobility wires. *Physical Review B* **51**, 13389-13402 (1985).

[2] R. N. Gurzhi. Hydrodynamic effects in solids at low temperatures. *Soviet Physics Uspekhi* **11**, 255 (1968).

[3] R. N. Gurzhi. Minimum of resistance in impurity-free conductors. *JETP* **17**, 521 (1963).

[4] R. Jaggi. Electron-fluid model for dc size effect. *Journal of Applied Physics* **69**, 816 (1991).

[5] L. W. Molenamp and M. J. M. Jong. Observation of knudsen and gurzhi transport regimes in a two-dimensional wire. *Solid State Electronics* **37**, 551-553 (1994).

[6] N. W. Ashcroft and N. D. Mermin. *Solid State Physics, p340-342,* (Harcourt College Publishers, London, 1976).

[7] E. M. Lifshitz and L. P. Pitaevskii. *Physical Kinetics, p1-26,* (Pergamon Press, Oxford, 1981).

[8] G. K. Batchelor. *An Introduction to Fluid Dynamics, p175-264,* (Cambridge University Press, Cambridge, 1981).

[9] G. Falkovich L. Levitov. Electron viscosity, current vortices and negative nonlocal resistance in graphene. *Nature Physics* **12**, 672-676 (2016).

[10] G. Falkovich and L. Levitov. Linking spatial distributions of potential and current in viscous electronics. *Physical Review Letters* **119**, 066601 (2017).

[11] F. M. D. Pellegrino, I. Torre, and A. K. Geim et al. Electron hydrodynamics dilemma: whirlpools or no whirlpools. *Physical Review B* **94**, 155414 (2016).

[12] D. A. Bandurin, I. Torre, and R. K. Kumar et al. Negative local resistance caused by viscous electron backflow in graphene. *Science* **351**, 1055-1058 (2016).

[13] P. J. W. Moll, P. Kushwaha, and N. Nandi et al. Evidence for hydrodynamic electron flow in PdCoO2. *Science* **351**, 1061-1064 (2016).

[14] J. Erdmenger, I. Matthaiakakis, and R. Meyer et al. Strongly coupled electron fluids in the poiseuille regime. *Physical Review B* **98**, 195143 (2018).

[15] H. Guo, E. Ilseven, G. Falkovich, and L. Levitov. Higher-than-ballistic conduction of viscous electron flows. `https://arxiv.org/abs/1607.07269` (2016).

[16] J. Crossno, J. K. Shi, and K. Wang et al. Observation of the dirac fluid and the breakdown of the wiedemann-franz law in graphene. *Science* **351**, 1058-1061 (2016) .

[17] K. S. Novoselov, A. K. Geim, and S. V. Morozov et al. Electric field effect in atomically thin carbon films. *Science* **306**, 666-669 (2004).

[18] K. S. Novoselov, A. K. Geim, and S. V. Morozov et al. Two-dimensional gas of massless dirac fermions in graphene. *Nature* **438**, 197-200 (2005).

[19] J. Zaanen. Electrons go with the flow in exotic material systems. *Science* **351**, 1026-1027 (2016) .

[20] A. S. Mayorov, R. V. Gorbachev, and S. V. Morozov et al. Micrometer-scale ballistic transport in encapsulated graphene at room temperature. *Nano Letters* **11**, 2396–2399 (2011).

[21] L. Wang, I. Meric, and P. Y. Huang et al. One-dimensional electrical contact to a two-dimensional material. *Science* **341**, 614-617 (2013) .

[22] L. D. Landau and E. M. Lifshitz. *Fluid Mechanics, p61-64, 3rd Ed.* (Pergamon Press, Oxford, 1966).

[23] I. Torre, A. Tomadin, and A. K. Giem et al. Nonlocal transport and the hydrodynamic shear viscosity in graphene. *Physical Review B* **92**, 165433 (2015).

[24] R. K. Kumar, D. A. Bandurin, and F. M. D. Pellegrino et al. Superballistic flow of viscous electron fluid through graphene constrictions. *Nature Physics* **13**, 1182–1185 (2017).

[25] A.V. Shytov, J. K. Fong, and G. Falkovich et al. Particle collisions and negative nonlocal response of ballistic electrons. *Physical Review Letters* **121**, 176805 (2018).

[26] D. A. Bandurin, A. V. Shytov, and L. S. Levitov et al. Fluidity onset in graphene. *Nature Communications* **9**, 4533 (2018).

[27] M. Shavit, A. V. Shytov, and G. Falkovich. Freely flowing currents and electric field expulsion in viscous electronics. `https://arxiv.org/abs/1812.10981` (2018).

[28] B. A. Braem, F. M. D. Pellegrino, and A. Principi et al. Scanning gate microscopy in a viscous electron fluid. *Physical Review B* **98**, 241304 (2018).

[29] L. Ella, A. Rozen, and J. Birkbeck et al. Simultaneous imaging of voltage and current density of flowing electrons in two dimensions. `https://arxiv.org/abs/1810.10744` (2018).

[30] A. V. Chaplik. Energy spectrum and electron scattering processes in inversion layers. *Soviet JETP* **33**, 997 (1971).

[31] G. F. Giuliani and J. J. Quinn. Lifetime of a quasiparticle in a two-dimensional electron gas. *Physical Review B* **26**, 4421 (1982).

[32] C. Kittel. *Introduction to Solid State Physics, p403-407, 8th Ed.* (John Wiley and Sons, New Deli, 2017).

[33] S. D. Gennaro and A. Rettori. On the electron-electron contribution to the low-temperature electrical resistivity of thin wires. *Journal of Physics F: Metal Physics* **15**, 2177-2188 (1985).

[34] J. Callaway. Model for lattice thermal conductivity at low temperatures. *Physical Review* **113**, 1046 (1959).

[35] M. R. Spiegel. *Schaum's Outlines of Theory and Problems of Complex Variables, p200-265, SI (Metric) Ed.* (McGraw-Hill Book Company, Singapore, 1981).

[36] R. V. Churchill. *Complex Variables and Applications, p183-211, 2nd Ed.* (McGraw-Hill Book Company, New

York, 1960).

[37] L. D. Landau and E. M. Lifshitz. *Mechanics, p1-5, 2nd Ed.* (Pergamon Press, Oxford, 1969).

[38] L. A. Ahlfors. *Complex Analysis: An Introduction to the Theory of Analytic Functions of One Complex Variable, p93-95, 2nd Ed.* (McGraw-Hill Book Company, New York, 1966).

[39] J. H. Lambert and D. L. Diaura. *Photometry, or, On the Measure and Graduations of light, colours and shade,* (Illuminating Engineering Society of North America, New York, 2001).

[40] W. H. Press, S. A. Teukolsky, W. T. Vetterling, and B. P. Flannery. *Numerical Recipes in C: The Art of Scientific Computing, p834-842, 2nd Ed.* (Cambridge University Press, New York, 2002).